Manganese silicate nanospheres-incorporated hydrogels : starvation therapy and tissue regeneration

Hongshi Ma [a,1], Qingqing Yu [a,b,1], Yu Qu [a,b], Yufang Zhu [a,b,*], Chengtie Wu [a,b,**]

[a] State Key Laboratory of High Performance Ceramics and Superfine Microstructure, Shanghai Institute of Ceramics, Chinese Academy of Sciences, 1295 Dingxi Road, Shanghai, 200050, China
[b] Center of Materials Science and Optoelectronics Engineering, University of Chinese Academy of Sciences, No,19(A) Yuquan Road, Beijing, 100049, China

A B S T R A C T

To prevent postoperative skin tumor recurrence and repair skin wound, a glucose oxidase (GOx)-loaded manganese silicate hollow nanospheres (MS HNSs)-incorporated alginate hydrogel (G/MS-SA) was constructed for starvation-photothermal therapy and skin tissue regeneration. The MS HNSs showed a photothermal conversion efficiency of 38.5%, and endowed composite hydrogels with satisfactory photothermal effect. Taking advantage of the catalytic activity of Mn ions, the composite hydrogels could decompose hydrogen peroxide (H_2O_2) into oxygen (O_2), which can alleviate the problem of tumor hypoxia microenvironment and endow GOx with an ability to consume glucose in the presence of O_2 for tumor starvation. Meanwhile, hyperthermia triggered by near infrared (NIR) irradiation could not only accelerate the reaction rate of H_2O_2 decomposition by MS HNSs and glucose consumption by GOx, but also ablate tumor cells. The anti-tumor results showed that synergistic effect of starvation-photothermal therapy led to the highest death rate of tumor cells among all groups, and its anti-tumor effect was obviously improved as compared with that of single photothermal treatment or starvation treatment. Interestingly, the introduction of MS HNSs into hydrogels could distinctly promote the epithelialization of the wound beds by releasing Mn ions as compared with the hydrogels without MS HNSs. It is expected that such a multifunctional platform with starvation-photothermal therapy will be promising for treating tumor-caused skin defects in combination of its regeneration bioactivity in the future.

1. Introduction

Surgical resection of skin tumors is often accompanied by long-term skin wound regeneration. Preventing tumor recurrence and repairing the damaged skin tissues are both required for patients with skin tumors to improve their postoperative life quality. In recent years, starvation therapy has been proved to be effective in suppressing tumor growth by blocking the energy (adenosine triphosphate, ATP) supply pathway of tumor cells [1–4]. Glucose oxidase (GOx) is a commonly used therapeutic agent in starvation therapy, in which GOx can oxidize intracellular glucose into gluconic acid and generate hydrogen peroxide (H_2O_2) under oxygen (O_2) supply and acid conditions [5–7]. However, hypoxic microenvironment in tumor sites seriously limits the glucose oxidation by GOx. In addition, for the tumor-induced skin defect regeneration, the reduced production of energy by starvation therapy may hinder the development of skin tissue regeneration, which requires a great deal of energy for cellular activity. To address these problems, it is of great significance to design and fabricate a multifunctional biomaterial with the ability of alleviating tumor hypoxia, and simultaneously improving skin wound repair.

It has been reported that manganese (Mn) ions can catalyze H_2O_2 decomposition to produce O_2 [8]. Taking advantage of both H_2O_2 oxidization product and energy shutting-off, MnO_2 nanomaterials combined with GOx have been applied in the multi-mode tumor therapies to

achieve satisfactory tumor therapeutic efficacy [1,9,10]. For example, a MnO_2-based nanoreactor with catalase-like activity has been designed to achieve continuous O_2 generation by combining photodynamic and starvation therapy [9]. Compared with photodynamic-starvation therapy, the high temperature induced by photothermal therapy (PTT) can improve the activity of GOx to obtain enhanced starvation therapy effect [11–13]. It is worth mentioning that Mn-ions containing biomaterials have emerged as potential photothermal agents for PTT, such as Mn-doped bioactive glass-ceramic [14] and MnO_2 nanosheets [15,16]. As far as we know, there are few studies about Mn-containing multifunctional biomaterials for the application of combined photothermal and starvation therapy [17].

In addition, promotion of re-epithelialization is one of cost-effective and safe options for faster regeneration of both acute and chronic wounds [18,19]. During the period of re-epithelialization, the keratinocytes start to continuously migrate from wound edges to wound bed until a complete epithelial layer is formed [20]. The cell behavior of keratinocytes can be regulated by integrin that is composed of α and β chain [21,22]. It has been reported that the manganese gluconate accelerates the migration of keratinocytes *in vitro* by elevating the expression of α3 and β1 subunits [23]. Clinical studies have found that manganese salts can promote the healing of cracked breasts [24]. However, the *in vivo* effect of Mn ions on wound healing has not been studied. On the other hand, it would be of great significance to investigate the postoperative tissue regeneration function of Mn-containing biomaterials, because Mn-containing nanoreactors have been extensively employed in killing tumor cells.

Considering that silicate biomaterials with excellent biocompatibility have great potential in skin tissue regeneration [25–27], we proposed to construct a multifunctional platform composed of manganese silicate hollow nanospheres (MS HNSs), GOx and sodium alginate (SA) hydrogels for combined tumor starvation-photothermal therapy and skin tissue regeneration. Here, MS HNSs were prepared *via* a hydrothermal method, then used to load GOx, and finally incorporated into SA hydrogel to obtain the composite hydrogels (G/MS-SA). The morphology, composition, photothermal performance, GOx-loading capacity and degradation behavior of MS HNSs were investigated. After MS HNSs were incorporated in hydrogels, the morphology, photothermal performance, catalytic property and glucose consumption activity of G/MS-SA hydrogels were explored. In addition, the starvation-photothermal therapeutic efficacy of G/MS-5SA hydrogels was investigated according to *in vitro* and *in vivo* anti-tumor experiments. Finally, the *in vivo* effects of G/MS-5SA hydrogels with and without NIR laser irradiation on a full-thickness skin wound model were evaluated.

2. Materials and methods

2.1. Preparation of MS HNSs and G/MS HNSs

Mesoporous silica nanoparticles (MSNs) were first prepared according to the previously reported reference [28] and used as templates. MSNs (0.05 g) and $Mn(CH_3COO)_2·4H_2O$ (0.05 g, Sigma-Aldrich) were then completely dispersed in deionized water (80 mL). The solution underwent hydrothermal treatment at 140 °C for 24 h. After the reaction solution cooled down, the precipitate was obtained by centrifugation and finally calcined at 650 °C for 6 h to obtain manganese silicate hollow nanospheres (MS HNSs).

MS HNSs (3 mg) were dispersed in the GOx (Sigma-Aldrich)-containing aqueous solution (1 mL, 2 mg/mL). The mixture was kept in a shaker (37 °C, 120 r/min) for 6 h. Finally, G/MS HNSs were obtained by centrifugation.

2.2. Preparation of composite hydrogels

Sodium alginate (SA) solution was fabricated by adding sodium

alginic acid salt (from brown algae, Sigma, 1.5 g) in deionized water (100 mL) at room temperature, followed by autoclave sterilization. MS HNSs were then uniformly dispersed in SA solution. The mixture was finally cross-linked with $CaCl_2$ solution (0.05 g/mL) to develop hydrogels. When the weight ratios of MS HNSs to sodium alginic acid salt were 1:20, 1:15, 1:10 and 1:5, the obtained hydrogels were named as MS-20SA, MS-15SA, MS-10SA and MS-5SA, respectively. The G/MS-5SA hydrogels were prepared when the weight ratio of G/MS HNSs to sodium alginic acid salt was 1:5. The SA hydrogels were prepared by the same process without the incorporation of MS HNSs.

2.3. Apparatus

Transmission electronic microscopy (TEM) was conducted on JEM-2100 F transmission electronic microscope (JEOL, Japan). Scanning electronic microscopy (SEM) and scanning transmission electron microscopy (STEM) observations were performed on Magellan 400 scanning electronic microscope (FEI, USA). X-ray diffraction (XRD) patterns were obtained by using Rigaku D/Max-2550V diffractometer (Geigerflex, Japan). X-ray photoelectron spectroscopy (XPS) was conducted on ESCALab250 (Thermo Fisher Scientific, USA). Specific surface area of the sample was determined by using Micromeritics ASAP 2010 analyzer (Micromeritics, USA). Fourier transform infrared spectroscopy (FTIR) was recorded on a spectrometer (Nicolet iS50, USA). The oxygen concentration in the solution was determined by a dissolved oxygen analyzer (JPBJ-609L, REX, China). The glucose content in medium was measured by glucose test strips (Sinocare, China). The wavelength of near infrared (NIR) laser was 808 nm (PM100D, Thorlabs GmbH, Germany). The temperature changes of the samples were recorded *via* an infrared-thermal imaging camera (A325sc, FLIR, USA). The released concentrations of Si and Mn elements in the solution were detected by inductively coupled plasma atomic emission spectrometry (ICP-AES, Vista AX, USA).

2.4. Characterization of MS HNSs

Photothermal performance of MS HNSs: MS HNSs suspension in aqueous solution (3 mg/mL) was irradiated with a NIR laser (power density: 0.2, 0.4, 0.6, and 0.8 W/cm^2) for 10 min. The temperature variations were recorded. The deionized water irradiated by 0.85 W/cm^2 laser was used as the control group. To quantify the photothermal conversion efficiency of MS HNSs, MS HNSs aqueous suspension (0.25 mL, 3 mg/mL) underwent 0.6 W/cm^2 irradiation for 350 s. Then, the laser was turned off and the suspension was cooled to room temperature. The temperature variations were recorded. Finally, the photothermal conversion efficiency was calculated according to the previous literature [29]. To investigate photothermal stability of MS HNSs, MS HNSs aqueous suspension (3 mg/mL) was irradiated with NIR laser at the power density of 0.5 W/cm^2 for 10 min and then the laser was turned off and the suspension was cooled down. This process was repeated four times and the temperature of suspension was monitored by an infrared-thermal imaging camera.

GOx-loading capacity of MS HNSs: 1 mg of MS HNSs were dispersed in different GOx (from Aspergillus niger, Sigma) aqueous solution (0.05, 0.1, 0.5, 1, 2, 3 mg/mL). The suspensions were kept in a shaker (37 °C, 120 r/min) for 6 h. After centrifugation, the GOx concentrations of supernatants (Cs) and original GOx aqueous (Co) were evaluated by BCA protein assay. The loading weight of GOx on MS HNSs was calculated as (Co–Cs) × 100%. The loading efficiency of GOx on MS HNSs was calculated as (Co–Cs)/Co × 100%.

Degradation behavior of MS HNSs: 3 mg of MS HNSs were dispersed in 30 mL of phosphate buffer solutions (PBS) with different pH values of 7.5, 6.5 and 5.5, respectively. The suspensions were kept in a shaker (37 °C, 120 r/min). After 1, 3, 6, 8, 12, 24, 60, 84 and 168 h, the suspensions were centrifuged. 6 mL of supernatant was collected, and 6 mL of fresh PBS was immediately added. The concentrations of Si and Mn

elements in the supernatants were detected by ICP AES. At 6 h and 24 h, the suspensions were centrifuged and the precipitations were obtained for TEM observation.

2.5. Characterization of hydrogels

Photothermal performance of hydrogels: The SA, MS-20SA, MS-15SA, MS-10SA, and MS-5SA hydrogels were put into 0.25 mL deionized water, and irradiated with NIR laser for 15 min at power density of 1 W/cm^2. The temperature variations were recorded *via* an infrared-thermal imaging camera.

Biocompatibility of hydrogels: Human dermal fibroblasts (HDFs) were cultured in Dulbecco's modified eagle medium (DMEM, Gibco) supplemented with 1% penicillin/streptomycin and 10% fetal bovine serum (HyClone). The third passage of 2.0×10^3 HDFs were seeded in each well of 24-well culture plate and cultured for 12 h. The SA, MS-20SA, MS-15SA, MS-10SA and MS-5SA hydrogels were gently placed in the transwells and co-cultured for 1, 3 and 5 days. At days 1, 3 and 5, the old medium was collected and HDFs were used for cell counting kit-8 (CCK-8, Kumamoto, Japan) test. The concentrations of Si and Mn elements in the collected medium were detected by ICP AES.

Catalytic property of hydrogels: MS-5SA hydrogels were put into 5, 2, 1 and 0.5 mmol/L H_2O_2 solutions (1 mL), respectively. The O_2 concentration in the solution was detected by an oxygen dissolved analyzer. SA hydrogel was put into 5 mmol/L H_2O_2 solution and the concentration of O_2 in the solution was measured as the control group. To evaluate the catalytic ability of hydrogels under NIR irradiation, MS-5SA hydrogels were put into 1 mmol/L H_2O_2 solution (0.4 mL), the temperatures of MS-5SA hydrogels were maintained at 37 °C, 45 °C and 50 °C by adjusting the power densities of NIR laser. The H_2O_2 solution was catalyzed by MS-5SA hydrogels at room temperature (23 °C), and the concentration of O_2 in the solution was measured as the control group.

Glucose consumption activity of hydrogels: Roswell Park Memorial Institute (RPMI) 1640 medium (Gibco) was selected as a glucose source. To explore the effect of different hydrogels on glucose consumption at room temperature (26 °C), SA, MS-SA and G/MS-SA hydrogels were placed into 0.5 mL of medium supplemented with H_2O_2 (10 mmol/L), respectively. The glucose content change was calculated according to glucose content in the medium, which was measured by glucose test strips every 20 s. To explore the effect of different photothermal temperatures on glucose consumption rate, G/MS-SA hydrogels were irradiated by NIR laser and maintained at 37, 42, 45 and 50 °C.

2.6. In vitro anti-tumor evaluation

B16F10 cells (murine melanoma cells) were cultured in RPMI 1640 medium supplemented with 1% penicillin/streptomycin and 10% fetal bovine serum. B16F10 cells were seeded in a 24-well culture plate with a density of 5.0×10^4 cells/well and cultured for 12 h. The SA, MS-20SA, MS-15SA, MS-10SA and MS-5SA hydrogels were gently placed in the transwells and co-cultured with B16F10 cells for 24 h. The viability of B16F10 cells was quantified by CCK-8 test at 450 nm. To explore the effects of starvation and photothermal therapy on the viability of B16F10 cells, the SA, MS-5SA and G/MS-5SA hydrogels were co-cultured with B16F10 cells. The MS-5SA and G/MS-5SA hydrogels were irradiated by 808 nm laser and kept at 42, 45 and 50 °C for 5 min, respectively. The temperature of hydrogels without irradiation was 37 °C. The survival rate of B16F10 cells was evaluated by using CCK-8 test. B16F10 cells after 45 °C irradiation for 5 min were stained with fluorescein isothiocyanate (FITC) to observe cytoskeleton and 4′,6-diamidino-2-phenylindole (DAPI) to observe cell nucleus using a confocal laser scanning microscope (CLSM, Leica TCS SP8, Germany).

2.7. In vivo anti-tumor evaluation

All the mice used in this study were purchased from Shanghai SLAC

Laboratory Animal Co., Ltd, China and fed in Shanghai Rat & Mouse Biotech Co., Ltd, China. The nude mice aged 6–7 weeks (Male, Balb/C) were selected for *in vivo* anti-tumor experiments. B16F10 melanoma cells (3.5×10^5) were injected into mice to establish a subcutaneous melanoma model. When the size of solid tumor was about 4 mm in diameter, a full-thickness skin wound (diameter: 10 mm) was created to expose the melanoma, which simulate the clinical wound caused by surgical resection of tumors. Solid tumors were not resected for more direct observation of tumor growth. There were seven groups (n = 5): Control, SA hydrogel without NIR laser (SA group), SA hydrogel with NIR laser (SA+L group), MS-5SA hydrogel without NIR laser (MS-5SA group), MS-5SA hydrogel with NIR laser (MS-5SA+L group), G/MS-5SA hydrogel without NIR laser (G/MS-5SA group) and G/MS-5SA hydrogel with NIR laser (G/MS-5SA+L group). From day 1 to day 3, 40 μL of SA, MS-5SA, and G/MS-5SA hydrogels were injected into solid tumors per day, respectively. The mice in the MS-5SA+L and G/MS-5SA+L groups received NIR irradiation and kept at about 45 °C (~1 W/cm^2) for 15 min per day for consecutive 3 days. The SA+L hydrogel was irradiated by NIR laser with the same power density (~1 W/cm^2). The temperatures of mice were monitored by NIR photothermal camera. After irradiation, 10 μL of SA, MS-5SA, and G/MS-5SA hydrogels were uniformly applied to wound sites in relative groups. The length (L) and width (W) of tumors at days 1, 3, 6, 8, 10, 12, and 14 were measured, and the relative tumor volume was calculated according to the previously reported study [30]. The photos of tumors and skin wounds at days 1, 3, 6, 10, and 14 were taken by a digital camera. At day 14, solid tumors in all groups were obtained, weighed and photographed. The new born skins were collected, photographed and treated with hematoxylin (H9627, Sigma, USA) and eosin (E4009, Sigma, USA) (H&E) staining. The detailed H&E staining method were described as follows. Firstly, samples were dewaxed with xylene solution for two times, and then dipped in gradient alcohol solutions (100%, 95%, 85% and 75%, respectively) and PBS solution. Secondly, samples were stained with hematoxylin and differentiated in 1% hydrochloric acid-75% alcohol solution; Thirdly, samples were steeped in 2% ammonia blue and stained with eosin. Finally, samples were dehydrated by alcohol, dipped in xylene solution, dropped with Permount TM Mounting Medium for mounting and observed *via* microscope.

2.8. In vivo wound healing

The C57BL/6 mice (male, 6–7 weeks) were divided into five groups (n = five): Control, SA group, MS-5SA group and G/MS-5SA group. A full-thickness skin wound (diameter: 15 mm) was created on the naked back of each mouse. From day 1 to day 3, 10 μL of SA, MS-5SA and G/MS-5SA hydrogel were uniformly applied to wound beds in relative groups, respectively. The wound beds at days 1, 3, 6, 9, 12 and 15 were photographed. The areas of skin wounds were measured using ImageJ. The areas of skin wounds at day t and day 0 were indicated as At and A0, respectively. The relative wound area was A_t/A_0 (%). The new skin tissues were collected and evaluated by H&E staining.

2.9. Statistical analysis

All data were showed as means ± standard deviation and were analyzed using a one-way analysis of variance (ANOVA) with a Student's *t*-test statistical analysis to evaluate the significance of differences. A *P*-value < 0.05 was considered statistically significant: *P < 0.05, **P < 0.01 and ***P < 0.001.

3. Results and discussion

3.1. Characterization of MS HNSs

MS HNSs were prepared *via* a hydrothermal method using mesoporous silica nanoparticles (MSNs) as templates. The morphology of MS

HNSs was characterized *via* transmission electron microscope (TEM) and scanning electron microscope (SEM). TEM image (Fig. 1a) showed hollow sphere-like nanostructures with the size of ~100 nm, which was similar in size to previous report [28]. The shells of MS HNSs were assembled by plenty of nanoparticles, showing rough and porous surfaces, which consisted of O, Mn and Si elements (Fig. 1b–e). According to scanning transmission electron microscope and its corresponding linear elemental analysis, we can see that MS HNSs had an obvious hollow structure and the internal diameter was ~50 nm (Figure S1). The X-ray diffraction (XRD) pattern of MS HNSs displayed the braunite phase ($Mn^{2+}Mn_6^{3+}SiO_{12}$, Figure S2) , and the corresponding XRD card is JCPDS#41–1367 [31]. The characteristic peaks of Mn, Si, and O elements on the surface of MS HNSs were detected using X-ray photoelectron spectroscopy (XPS) (Fig. 1f). The XPS characteristic spectrum for Mn 2p3 showed that the Mn^{3+}/Mn^{2+} atomic ratio was ~2.35 (Fig. 1g).

The heating curves of MS HNSs suspensions under NIR irradiation were exhibited in Fig. 1h. The suspension temperature increased with the increase of power densities of NIR laser. The steady-state temperature of the MS HNSs suspension could reach ~75 °C (power density: 0.8 W/cm^2), while negligible temperature variation was observed in the group of water without MS HNSs, suggesting that MS HNSs could convert the NIR-laser energy to heat. On the basis of the results of the plateau-state temperature and time constant for heat transfer (Figure S3), the photothermal conversion efficiency of MS HNSs was calculated to be ~38.5%, which was higher than that of MnO_2 nanosheets (21.4%) [15] and Mn-doped iron oxide nanoparticles (28.8%) [32], indicating that MS HNSs were outstanding candidates for
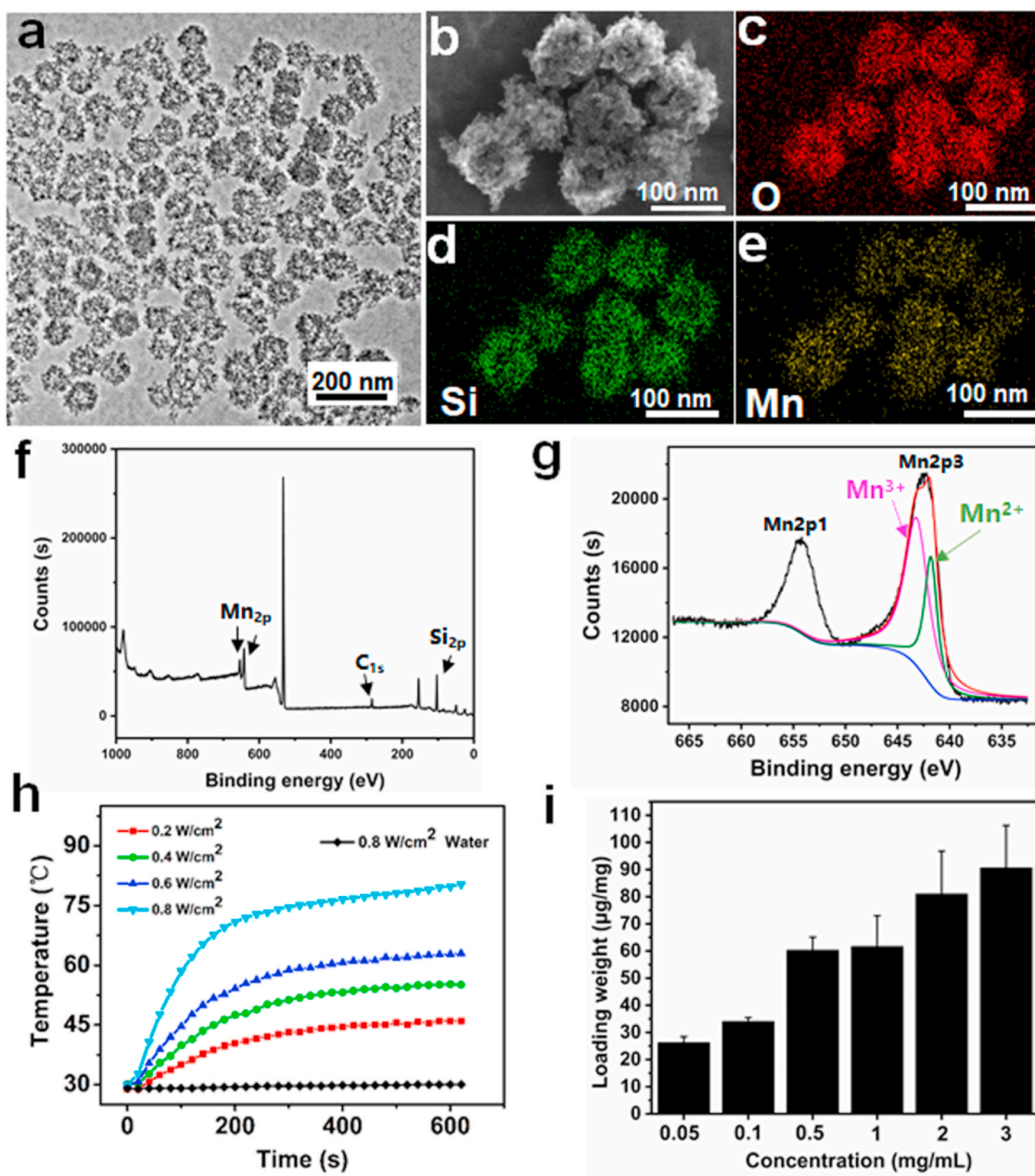

Fig. 1. Characterization of MS HNSs: (a) TEM image; (b) SEM image and (c–e) the corresponding elemental mapping images; (f) XPS spectrum; (g) XPS characteristic spectrum for Mn 2p; (h) the temperature variation curves of MS HNSs aqueous suspension irradiated under a NIR laser (laser power densities: 0.2, 0.4, 0.6 and 0.8 W/cm²); (i) the loading weight of GOx on MS HNSs in different GOx concentrations (0.05, 0.1, 0.5, 1, 2 and 3 mg/mL). MS HNSs were excellent photothermal agents and GOx carriers.

photothermal therapy.

As shown in Figure S4, photothermal stability results demonstrated that MS HNSs was mechanically robust and chemically stable under high temperature and can act as a photothermal agent with stable photothermal performance. The specific surface area of MS HNSs was 448.6 m^2/g (Figure S5), which offered the possibility of MS HNSs in loading GOx. The GOx-loading capacity of MS HNSs was investigated by dispersing MS HNSs into GOx-containing solutions with different GOx concentrations. It was found that the content of GOx adsorbed on MS HNSs increased with the increase of GOx concentration from 0.05 mg/mL to 3 mg/mL (Fig. 1i, Figure S6). When the concentration of GOx was 2 mg/mL, the loading capacity and the loading efficiency of GOx were ~81 µg/mg and ~8.44%, respectively. Besides the large specific surface area of MS HNSs, the high GOx-loading capacity might be ascribed to the hydroxyl groups (Si–OH and Mn–OH, Figure S7) that can adsorb GOx molecules by hydrogen bonds [33]. Therefore, MS HNSs could be applied as excellent photothermal agents and GOx carriers.

The stability of MS HNSs was evaluated by *in vitro* degradation experiments in phosphate buffer solutions (PBS) (pH: 7.5, 6.5 and 5.5, respectively). MS HNSs were soaked in PBS (pH 7.5 and 5.5) for 6 h and 24 h, and then collected for TEM observations. It showed that MS HNSs maintained the complete spherical morphology to a large extent, after 24 h incubation under neutral condition (Figure S8a-b), but the spherical morphology of MS HHSs had a certain degree of collapse after 24 h incubation under acidic condition (pH 5.5, Figure . S8c-d). The spherical morphology of MS HNSs was more stable in neutral solution than that in acidic solution, because Mn–O bonds in the chemical constitution of MS HNSs are easily broken in acidic solution [34]. In addition, the released concentration of Mn and Si ions were monitored *via* ICP AES during degradation. The release rate of Mn ions from MS HNSs in acidic PBS was more rapid than that in neutral PBS (Figure S8e-f). The concentrations of Mn ions after 24 h of degradation were 14.28 µg/mL at pH 7.5 and 32.36 µg/mL at pH 5.5, respectively. However, such high-concentration Mn ions may have a certain degree of cytotoxicity. Previous studies have reported that Mn ions with a concentration of >0.1 mM/mL (5.494 µg/mL) significantly inhibit the proliferation of osteoblasts [35]. Inspired by the results that hydrogel can accommodate the nanoparticles and slow down the ion release rates [36],
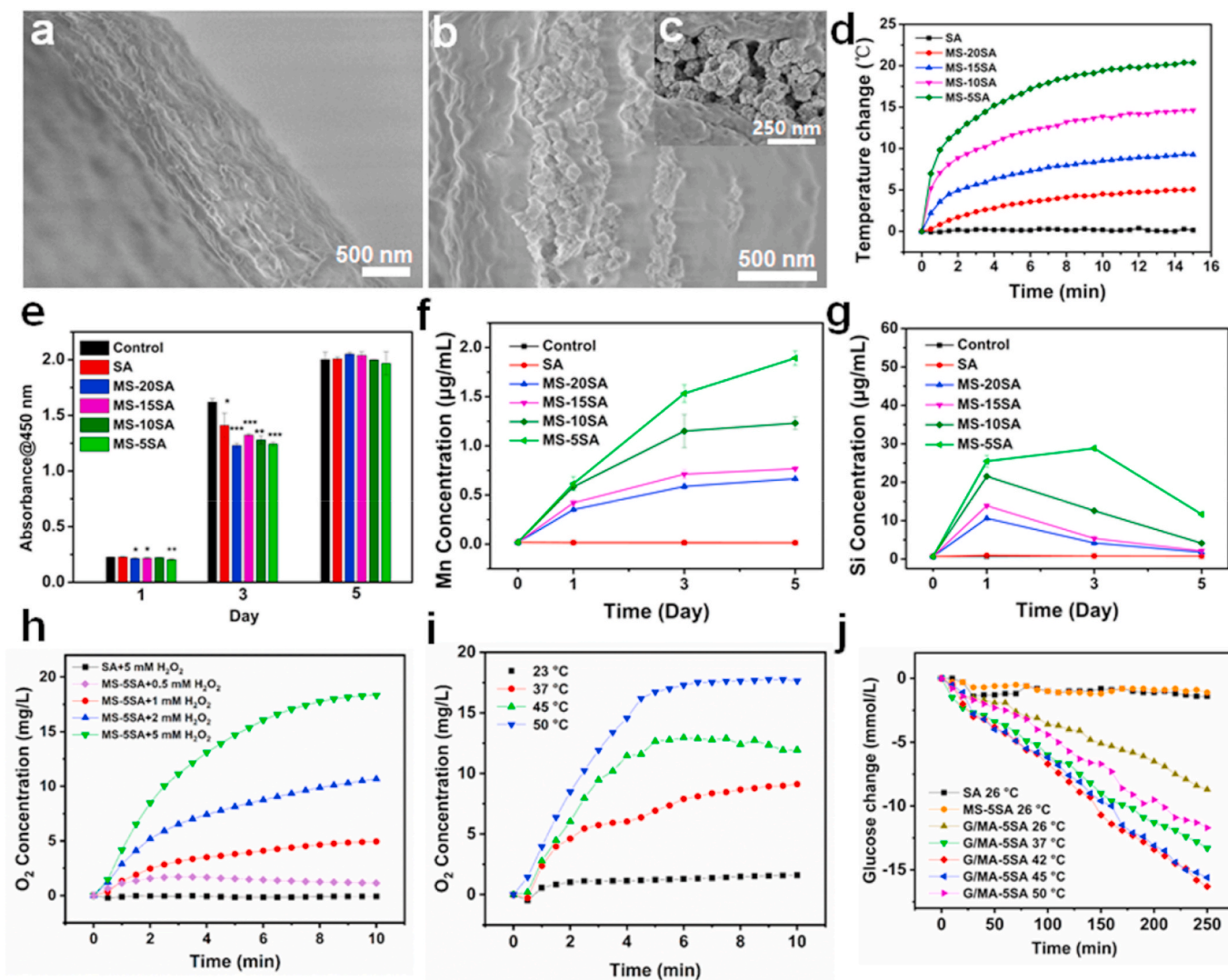

Fig. 2. Characterizations of MS HNSs-incorporated SA hydrogels. SEM images of (a) SA hydrogels and (b, c) MS-5SA hydrogels; (d) the temperature change curves of different hydrogels under 1 W/cm² laser irradiation for 15 min; (e) the cell viabilities of HDFs after co-incubation with different hydrogels for 1, 3 and 5 days; the release profiles of (f) Mn and (g) Si elements from different hydrogels during co-incubation; (h) the oxygen generation curves in different H_2O_2 solution with different concentrations of 0.5, 1, 2, 5 mmol/L; (i) NIR-triggered oxygen generation curves under different irradiation temperature of 37 °C, 45 °C and 50 °C; (j) the glucose concentration changes under different irradiation temperature of 37 °C, 42 °C, 45 °C and 50 °C. MS HNSs incorporated in hydrogels endowed the composite hydrogels with perfect photothermal effect, catalytic performance, and glucose consumption activity.

incorporating MS HNSs into biocompatible hydrogel matrix would be a promising strategy to decrease toxicity of Mn ions.

3.2. Characterization of MS HNSs-incorporated hydrogels

Considering that the fast biodegradation of MS HNSs may cause potential cytotoxicity, MS HNSs with different contents were incorporated in biocompatible sodium alginic acid salt to prepare MS-20SA, MS-15SA, MS-10SA and MS-5SA hydrogels (Figure S9). The freeze-dried SA and MS-5SA hydrogels were observed under SEM. As shown in Fig. 2a–c, MS HNSs were embedded in SA hydrogels and the nanostructures of MS HNSs were not destroyed. The effect of MS HNSs content on photothermal performance of composite hydrogels was further evaluated. The results showed that the steady-state temperature of SA, MS-20SA, MS-15SA, MS-10SA and MS-5SA hydrogels in 0.25 mL water increased by ~0.3, 5.1, 9.3, 14.6 and 20.4 °C under 1 W/cm^2 irradiation for 15 min, respectively (Fig. 2d). It was showed that the steady-state temperature of the composite hydrogels elevated with increasing the content of MS HNSs, while the temperature of pure SA hydrogel had no obvious increase, indicating that the photothermal ability of composite hydrogels was related with MS HNSs content.

Skin fibroblasts are the main structural components of skin dermis and play an important role in synthesizing collagen fibers [37]. To investigate the cytocompatibility of the composite hydrogels, the cell proliferation of human dermal fibroblasts (HDFs) was evaluated after co-culturing with SA, MS-20SA, MS-15SA, MS-10SA and MS-5SA hydrogels for 1, 3 and 5 days. The proliferation of HDFs showed an increasing trend within 5 days and there was no obvious difference in cell viability among all groups at day 5 (Fig. 2e). The MS HNSs-incorporated hydrogels showed excellent cytocompatibility even at a high concentration of MS HNSs. The release profiles of Mn ions and Si ions from different composite hydrogels during cell incubation were shown in Fig. 2f and g. The Mn concentrations of the MS-5SA group were 0.61, 1.53 and 0.89 g/mL at 1, 3 and 5 days, respectively. And the Si concentrations of the MS-5SA group were 25.47, 28.85 and 11.66 g/mL at 1, 3 and 5 days, respectively. Owing to the MS HNSs-content-dependent photothermal properties of composite hydrogels, the MS-5SA hydrogels were used for subsequent experiments in order to easily meet the temperature requirements of photothermal treatment.

It is well known that Mn ions (Mn^{2+} and Mn^{3+}) have outstanding catalytic activity and can catalyze the decomposition of H$_2$O$_2$ into O$_2$ and H$_2$O [8,38]. Since chemical composition of MS HNSs included Mn^{2+} and Mn^{3+} ions, the catalytic activity of MS-5SA hydrogels in decomposing H$_2$O$_2$ was evaluated by measuring O$_2$ concentration in the solution. It is shown that the O$_2$ concentration in SA group showed no visible variation even at a high H$_2$O$_2$ concentration of 5 mmol/L (Fig. 2h). However, MS-5SA hydrogels could decompose H$_2$O$_2$ to produce O$_2$ at a low H$_2$O$_2$ concentration of 0.5 mmol/L, and the content of O$_2$ increased with elevating H$_2$O$_2$ concentration. To investigate whether the temperature will affect the catalytic efficiency, the H$_2$O$_2$ decomposition performance of MS-5SA hydrogels under NIR stimulation was further explored at 37 °C, 45 °C and 50 °C, taking advantage of photothermal heating effect of MS-5SA hydrogels. The results showed that the decomposition rate of H$_2$O$_2$ raised with increasing NIR-triggered temperature, since the hyperthermia could accelerate the decomposition process (Fig. 2i).

The glucose consumption activity of G/MS-5SA hydrogels was investigated under different photothermal temperatures. G/MS-SA hydrogels were irradiated by NIR laser and maintained at 37 °C, 42 °C, 45 °C and 50 °C, respectively. As shown in Fig. 2j, when the temperature was lower than 42 °C, the increase of temperature could accelerate the reaction of GOx consuming glucose; when the temperature was higher than 42 °C, the activity of GOx gradually decreased with the increase of temperature. It is likely that the optimum temperature of enzyme activity is 42 °C. Therefore, MS HNSs embedded in hydrogels

endowed the composite hydrogels with perfect catalytic performance and glucose consumption activity.

3.3. In vitro anti-tumor effects of G/MS-5SA hydrogels

The efficacy of *in vitro* photothermal therapy and tumor starvation therapy of G/MS-5SA hydrogels was explored on mouse skin melanoma cells (B16F10 cells) by treating them with SA, MS-5SA, G/MS-5SA, MS-5SA+Laser (42 °C, 45 and 50 °C) and G/MS-5SA+Laser (42 °C, 45 and 50 °C), respectively. The cell viability of B16F10 cells was shown in Fig. 3a. Without NIR irradiation (37 °C), the average cell survival rates of SA, MS-5SA and G/MS-5SA groups were about 93.6%, 93.8% and 35.6% as compared to the Control group (100%), respectively. It was revealed that MS HNSs in the hydrogels showed no significant killing effects on B16F10 cells, while the GOx-loaded MS HNSs could obviously killing tumor cells. When the GOx was applied, the cell survival rate of B16F10 cells in G/MS-5SA group was significantly reduced. Since rapid proliferation of tumor cells requires a great deal of energy and is heavily dependent on energy supply (glucose), once tumor cells fail to uptake nutrient to feed themselves, they will starve to death [39,40]. Therefore, the insufficient glucose limited the rapid proliferation of tumor cells. When the irradiation temperatures were at 42 °C, 45 °C and 50 °C, the average survival rates of tumor cells in G/MS-5SA groups were ~17.2%, 6.9% and 2.7%, respectively, while ~94.6%, 71.7% and 55.0% in MS-5SA groups. The results indicated that the increasing irradiation temperature increased mortality of tumor cells and simultaneously higher temperature promoted the activity of starvation therapy, and then induced more tumor cell mortality, showing that synergetic therapy had a more effective therapy effect. It is well accepted that the tumor cell death starts to appear when the incubation temperature is higher than 43 °C [41,42] and the higher irradiation temperature leads to the higher mortality of tumor cells [43,44]. The superior cell-killing effects of G/MS-5SA hydrogels under NIR irradiation evidently resulted from the combination of the MS HNSs-triggered photothermal therapy and GOx-triggered tumor starvation therapy. Furthermore, the anti-tumor efficacy after different treatments was explored by using cell nuclei/-cytoskeleton fluorescence staining. Fewer surviving cells appeared in the G/MS-5SA+L group than in the MS-5SA+L group and G/MS-5SA group, further demonstrating the synergistic anti-tumor effect of combined starvation and photothermal therapy (Fig. 3b). Therefore, G/MS-5SA hydrogels irradiated under NIR laser could significantly kill tumor cells *in vitro* through glucose consumption by GOx and hyperthermia by MS HNSs.

3.4. In vivo anti-tumor effects of G/MS-5SA hydrogels

The intriguing *in vitro* synergistic anti-tumor results encourage the further assessment of combined starvation and photothermal therapy against *in vivo* solid tumors. The mice bearing B16F10 melanoma tumor were divided into seven groups randomly: Control, SA, SA+L, MS-5SA, MS-5SA+L, G/MS-5SA and G/MS-5SA+L. The temperature of tumor surface in the MS-5SA+L and G/MS-5SA+L groups were ~45 °C, while ~38 °C was achieved in the SA+L group (Fig. 4a). From day 1 to day 3, the NIR laser was applied for 15 min every day. The relative tumor volume within 14 days was recorded. The results showed that the tumor tissues in the G/MS-5SA+L group was continuously inhibited within 14 days, while solid tumors in the MS-5SA+L group began to grow slowly at day 8, and solid tumors in the G/MS-5SA group began to grow rapidly at day 6 (Fig. 4b). The photos (Fig. 4c) and weights (Figure S10) of the resected tumors at day 14 showed that the tumor tissues in G/MS-5SA+L group were the smallest, suggesting that G/MS-5SA+L treatment effectively killed tumor cells *in vivo*, and its anti-tumor effect was much better than that of MS-5SA+L and G/MS-5SA groups.

Besides the observation of tumor growth, the wound beds above the tumors were photographed (Fig. 4d). The results showed that after the treatment of tumor photothermal/starvation therapy, the solid tumor in
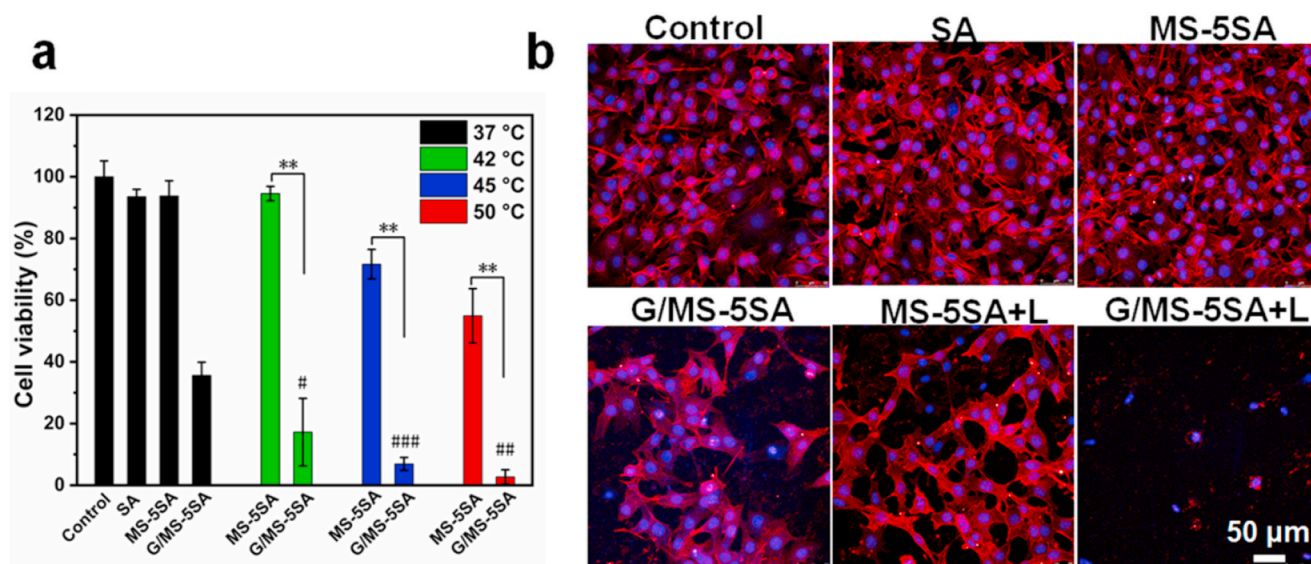
Fig. 3. *In vitro* anti-tumor efficiency of different hydrogels. (a) Cell viability of B16F10 cells without NIR irradiation (37 °C) and with different NIR irradiation (42 °C, 45 °C and 50 °C) for 5 min; (b) the corresponding confocal laser scanning microscopy images of tumor cells in different groups. The G/MS-5SA+L group showed a higher cell-killing efficiency than the G/MS-5SA and MS-5SA+L groups. The G/MS-5SA hydrogels irradiated by NIR laser could significantly kill tumor cells *in vitro* through glucose consumption by GOx and hyperthermia by MS HNSs.
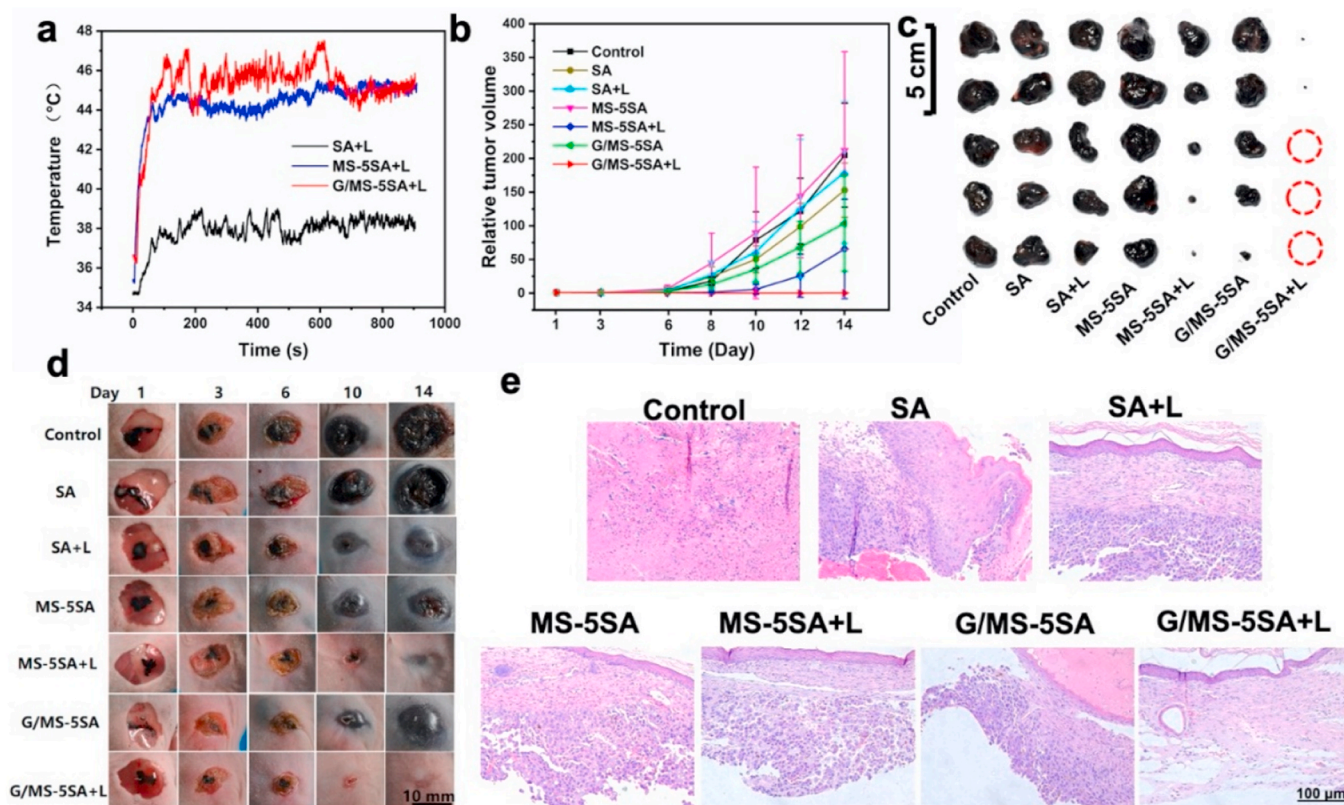

Fig. 4. *In vivo* anti-tumor efficiency of different hydrogels. (a) The temperature changes of tumors treated with the laser-irradiated SA, MS-5SA and G/MS-5SA hydrogels (~1 W/cm², 15 min); (b) tumor growth curves in a period of 14 days; (c) photographs of the excised tumors at day 14 (the red dotted circles represents the disappeared tumors); (d) photographs of tumors and skin wounds at day 1, 3, 6, 10 and 14; (e) hexatoxylin and eosin staining of the newly formed skin tissues. G/MS-5SA hydrogels with irradiation exhibited a high *in vivo* anti-tumor efficacy in suppressing tumor growth by combining photothermal therapy with starvation therapy. (For interpretation of the references to colour in this figure legend, the reader is referred to the Web version of this article.)

the G/MS-5SA+L group disappeared, and the skin wound healed gradually. While, in the other six groups, the skin wound was still visible without healing tendency. The images of the inner side of the newly

formed skin (Figure S11) showed that there were no visible tumor tissues in the G/MS-5SA+L group. In contrast, a bulk of tumor tissues was clearly observed in other six groups. In order to explore whether the

melanoma cells grew in newly formed skin layers, the skin slices were further observed after hexatoxylin and eosin (H&E) staining. The results displayed that the G/MS-5SA+L group had no visible tumor cells in the newly regenerated skin (Fig. 4e), which further illustrated that the laser irradiated G/MS-5SA hydrogels could possess a high *in vivo* anti-tumor efficacy in suppressing tumor growth through combining heat treatment with starvation therapy. The results above suggest that starvation-photothermal therapy exhibited satisfactory tumor therapy effect *in vivo* and its anti-tumor effect was much better than that of single photothermal treatment or starvation treatment. The reasons are as follows. First, photothermal therapy, as an efficient tumor therapy method, can induce protein denaturation, cell membrane damage, cell apoptosis and necrosis [45–47]. Second, the corresponding rise in temperature induced by photothermal therapy can accelerate the activity of GOx [17]. The improved catalytic efficiency of GOx can promote the consumption of glucose and generation of H_2O_2, further enhance starvation therapy [48].

3.5. In vivo wound healing effects of G/MS-5SA hydrogels

Aiming at postoperative management of resection of skin tumors, preventing tumor recurrence is the primary task. However, the healing of resection-caused skin defects are always neglected [49]. Biomaterials that can accelerate the repair of skin defect on the premise of eradicating tumor cells are need. Therefore, to investigate the *in vivo* effect of G/MS-5SA hydrogels on wound healing, the simulated surgical wounds were treated by the Control, SA group, MS-5SA group and G/MS-5SA group, respectively. The wound healing rate was evaluated by measuring the wound area. The results showed that all wounds were scabby at day 15 (Fig. 5a) and the relative wound areas at day 15 have no obvious difference among all groups. At day 12, the relative wound areas in MS-5SA group (15.7%) displayed obviously smaller than that of the SA (38.5%), and G/MS-5SA (22.9%) groups (Fig. 5b). It is likely that the GOx might destroy glucose metabolism and inhibit ATP production, however, a large amount of ATP is required for skin tissue regeneration. Therefore, the relative wound area in the G/MS-5SA group may be slightly larger than that of the MS-5SA group. H&E staining of skin slices was further performed to show the effectiveness of *in vivo* wound healing effects from a microscopic perspective. As shown in Fig. 5c, an intact sheet of epithelial layer was generated under the scab in the MS-5SA group, while no obvious epithelial layer was observed in the Control and SA group. It is likely that bioactive Mn ions released from MS-5SA hydrogel could promote the migration of keratinocytes, the wound recovery effect in the MS-5SA group was better than that in the Control and SA group. It has reported that keratinocytes can be regulated by integrin, composed of α and β chain [21,22]. And Mn ions can promote the migration of keratinocytes by stimulating the expression of α3 and β1 subunits [23]. Comparatively, GOx in the composite hydrogels compromised the re-epithelization function of MS HNSs because of glucose consumption in the G/MS-5SA group. However, compared with SA group, the repair quality of the wounds treated by G/MS-5SA hydrogels was much better even in the presence of GOx at day 12.
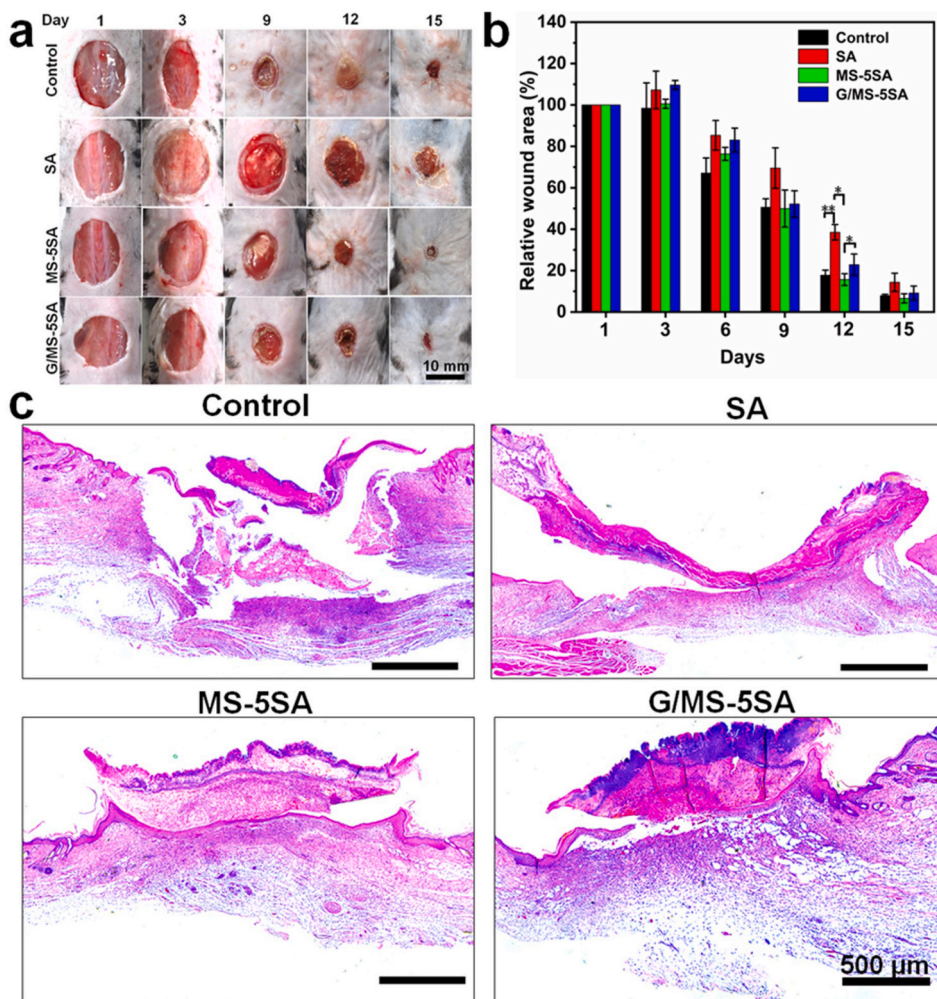

Fig. 5. *In vivo* skin tissue regeneration. (a) Wound photographs and (b) wound healing efficiency in different groups; (c) H&E staining of the newly formed skin tissues. MS HNSs in the composite hydrogels could promote the wound recovery rate and reduced the side effect of GOx.

Therefore, the side effect of GOx could be weakened by the therapeutic MS HNSs. The tumor treatments are always not conducive to the subsequent tissue regeneration, since healthy cells are damaged to some extent during tumor therapy. The future efforts are necessary to make to regulate the balance between tumor treatments and tissue regeneration.

4. Conclusions

In summary, a multifunctional hydrogel incorporated with GOx-loaded MS HNSs were successfully constructed as a platform for tumor starvation-photothermal therapy and tissue regeneration. MS HNSs exhibited excellent photothermal performance and GOx-loading capacity. The MS HNSs-incorporated hydrogels showed MS HNSs-content-dependent photothermal performance. Furthermore, MS HNSs endowed the composite hydrogels with catalytic activity and could decompose H_2O_2 to produce O_2 to optimize tumor microenvironment. The photothermal heating could accelerate H_2O_2 decomposition and glucose consumption. In anti-tumor experiments, the laser-irradiated G/MS-5SA hydrogels rapidly killed the *in vitro* tumor cells and inhibited *in vivo* tumor growth by combined starvation and photothermal therapy. When G/MS-5SA hydrogels were implanted into the wound sites, the bioactive Mn ions released from G/MS-5SA hydrogels could promote the epithelialization of the wounds and reduced the side effect of GOx treatments. Hence, the MS HNSs-incorporated hydrogels with synergistic starvation-photothermal therapy and skin tissue regeneration activity may have great potential for postoperative management of resection of skin tumors.

Author contributions

All authors have given approval to the final version of the manuscript. Hongshi Ma[1] and Qingqing Yu[1] contributed equally to this work.

CRediT authorship contribution statement

Hongshi Ma: Visualization, Writing – original draft, Formal analysis, Validation. **Qingqing Yu:** Investigation, Writing – original draft, Methodology, Conceptualization. **Yu Qu:** Resources. **Yufang Zhu:** Project administration, Writing – review & editing. **Chengtie Wu:** Funding acquisition, Supervision, Writing – review & editing.

Declaration of competing interest

The authors declare no competing financial interest.

Acknowledgements

Appendix A. Supplementary data

Supplementary data to this article can be found online at https://doi.org/10.1016/j.bioactmat.2021.04.042.

References

[1] X. Yang, Y. Yang, F. Gao, J.J. Wei, C.G. Qian, M.J. Sun, Biomimetic hybrid nanozymes with self-supplied H(+) and accelerated O2 generation for enhanced starvation and photodynamic therapy against hypoxic tumors, Nano Lett. 19 (2019) 4334–4342.

[2] Z. Yu, P. Zhou, W. Pan, N. Li, B. Tang, A biomimetic nanoreactor for synergistic chemiexcited photodynamic therapy and starvation therapy against tumor metastasis, Nat. Commun. 9 (2018) 5044.

[3] M.K. Zhang, C.X. Li, S.B. Wang, T. Liu, X.L. Song, X.Q. Yang, J. Feng, X.Z. Zhang, Tumor starvation induced spatiotemporal control over chemotherapy for synergistic therapy, Small 14 (2018), e1803602.

[4] C. Zhang, D. Ni, Y. Liu, H. Yao, W. Bu, J. Shi, Magnesium silicide nanoparticles as a deoxygenation agent for cancer starvation therapy, Nat. Nanotechnol. 12 (2017) 378–386.

[5] L.H. Fu, C. Qi, J. Lin, P. Huang, Catalytic chemistry of glucose oxidase in cancer diagnosis and treatment, Chem. Soc. Rev. 47 (2018) 6454–6472.

[6] S.Y. Li, H. Cheng, B.R. Xie, W.X. Qiu, J.Y. Zeng, C.X. Li, S.S. Wan, L. Zhang, W.L. Liu, X.Z. Zhang, Cancer cell membrane camouflaged cascade bioreactor for cancer targeted starvation and photodynamic therapy, ACS Nano 11 (2017) 7006–7018.

[7] W. Zhao, J. Hu, W. Gao, Glucose oxidase-polymer nanogels for synergistic cancer-starving and oxidation therapy, ACS Appl. Mater. Interfaces 9 (2017) 23528–23535.

[8] M. Wekesa, Y. Ni, Further understanding of the chemistry of manganese-induced peroxide decomposition, Can. J. Chem. Eng. 81 (2008) 968–972.

[9] W. Pan, Y. Ge, Z. Yu, P. Zhou, B. Cui, N. Li, B. Tang, A cancer cell membrane-encapsulated MnO2 nanoreactor for combined photodynamic-starvation therapy, Chem. Commun. 55 (2019) 5115–5118.

[10] Y. Zhang, H. Wang, X. Jia, S. Du, Y. Yin, X. Zhang, Cascade catalytic nanoplatform for enhanced starvation and sonodynamic therapy, J. Drug Target. 28 (2020) 195–203.

[11] C. Liu, C. Li, Y. Qian, L. Hu, J. Fang, W. Tong, R. Nie, Q. Chen, H. Wang, Magnetic-induced graphene quantum dots for imaging-guided photothermal therapy in the second near-infrared window, Biomaterials 232 (2020) 119700.

[12] F. Ding, X. Gao, X. Huang, H. Ge, M. Xie, J. Qian, J. Song, Y. Li, X. Zhu, C. Zhang, Polydopamine-coated nucleic acid nanogel for siRNA-mediated low-temperature photothermal therapy, Biomaterials 245 (2020) 119976.

[13] Y. Chen, Z.H. Li, P. Pan, J.J. Hu, S.X. Cheng, X.Z. Zhang, Tumor-microenvironment-triggered ion exchange of a metal-organic framework hybrid for multimodal imaging and synergistic therapy of tumors, Adv. Mater. 32 (2020), e2001452.

[14] Y. Liu, T. Li, H. Ma, D. Zhai, C. Deng, J. Wang, S. Zhuo, J. Chang, C. Wu, 3D-printed scaffolds with bioactive elements-induced photothermal effect for bone tumor therapy, Acta Biomater. 73 (2018) 531–546.

[15] Z. Liu, S. Zhang, H. Lin, M. Zhao, H. Yao, L. Zhang, W. Peng, Y. Chen, Theranostic 2D ultrathin MnO2 nanosheets with fast responsibility to endogenous tumor microenvironment and exogenous NIR irradiation, Biomaterials 155 (2018) 54–63.

[16] L. Wang, S. Guan, Y. Weng, S.M. Xu, H. Lu, X. Meng, S. Zhou, Highly efficient vacancy-driven photothermal therapy mediated by ultrathin MnO2 nanosheets, Acs Appl. Mater. Inter. 11 (2019) 6267–6275.

[17] T. He, H. Xu, Y. Zhang, S. Yi, R. Cui, S. Xing, C. Wei, J. Lin, P. Huang, Glucose oxidase-instructed traceable self-oxygenation/hyperthermia dually enhanced cancer starvation therapy, Theranostics 10 (2020) 1544–1554.

[18] H.S. Kim, N.H. Kim, J. Kim, I.H. Cha, Inducing re-epithelialization in skin wound through cultured oral mucosal keratinocytes, J. Korean Assoc. Oral Maxillofac. Surg. 39 (2013) 63–70.

[19] R. Xu, G. Luo, H. Xia, W. He, J. Zhao, B. Liu, J. Tan, J. Zhou, D. Liu, Y. Wang, Z. Yao, R. Zhan, S. Yang, J. Wu, Novel bilayer wound dressing composed of silicone rubber with particular micropores enhanced wound re-epithelialization and contraction, Biomaterials 40 (2015) 1–11.

[20] D. Harper, A. Young, C.-E. McNaught, The physiology of wound healing, Surgery 32 (2014) 445–450.

[21] R.O. Hynes, Integrins: versatility, modulation, and signaling in cell adhesion, Cell 69 (1992) 11–25.

[22] D.J. Geer, D.D. Swartz, S.T. Andreadis, Fibrin promotes migration in a three-dimensional in vitro model of wound regeneration, Tissue Eng. 8 (2002) 787–798.

[23] I. Tenaud, S. Leroy, N. Chebassier, B. Dreno, Zinc, copper and manganese enhanced keratinocyte migration through a functional modulation of keratinocyte integrins, Exp. Dermatol. 9 (2000) 407–416.

[24] J. Barrat, G. Crepin, Y. Darbois, S. Sirot, Copper and manganese gluconate in the treatment of breast fissures during breast feeding, Rev. Fr. Gynecol. Obstet. 87 (1992) 49–51.

[25] Q. Yu, J. Chang, C. Wu, Silicate bioceramics: from soft tissue regeneration to tumor therapy, J. Mater. Chem. B 7 (2019) 5449–5460.

[26] H. Ma, Q. Zhou, J. Chang, C. Wu, Grape seed-inspired smart hydrogel scaffolds for melanoma therapy and wound healing, ACS Nano 13 (2019) 4302–4311.

[27] F. Lv, J. Wang, P. Xu, Y. Han, H. Ma, H. Xu, S. Chen, J. Chang, Q. Ke, M. Liu, Z. Yi, C. Wu, A conducive bioceramic/polymer composite biomaterial for diabetic wound healing, Acta Biomater. 60 (2017) 128–143.

[28] M. Shi, Y. Zhou, J. Shao, Z. Chen, B. Song, J. Chang, C. Wu, Y. Xiao, Stimulation of osteogenesis and angiogenesis of hBMSCs by delivering Si ions and functional drug from mesoporous silica nanospheres, Acta Biomater. 21 (2015) 178–189.

[29] B. Li, F. Yuan, G. He, X. Han, X. Wang, J. Qin, Z.X. Guo, X. Lu, Q. Wang, I.P. Parkin, C. Wu, Ultrasmall CuCo2S4 nanocrystals: all-in-one theragnosis nanoplatform with magnetic resonance/near-infrared imaging for efficiently photothermal therapy of tumors, Adv. Funct. Mater. 27 (2017), 1606218.

[30] X. Wang, T. Li, H. Ma, D. Zhai, C. Jiang, J. Chang, J. Wang, C. Wu, A 3D-printed scaffold with MoS2 nanosheets for tumor therapy and tissue regeneration, NPG Asia Mater. 9 (2017) e376-e376.

[31] C.C. Yec, H.C. Zeng, Nanobubbles within a microbubble: synthesis and self-assembly of hollow manganese silicate and its metal-doped derivatives, ACS Nano 8 (2014) 6407–6416.

[32] Y. Fu, X. Li, H. Chen, Z. Wang, W. Yang, H. Zhang, CXC chemokine receptor 4 antagonist functionalized renal clearable manganese-doped iron oxide nanoparticles for active-tumor-targeting magnetic resonance imaging-guided bio-photothermal therapy, ACS Appl. Bio Mater. 2 (2019) 3613–3621.

[33] C. Wu, Y. Zhang, X. Ke, Y. Xie, H. Zhu, R. Crawford, Y. Xiao, Bioactive mesopore-glass microspheres with controllable protein-delivery properties by biomimetic surface modification, J. Biomed. Mater. Res. 95 (2010) 476–485.

[34] L. Yu, Y. Chen, "Manganese extraction" strategy enables tumor-sensitive biodegradability and theranostics of nanoparticles, Nanomed. Nanotechnol. Biol. Med. 14 (2018) 1850.

[35] F. Luthen, U. Bulnheim, P.D. Muller, J. Rychly, H. Jesswein, J.G. Nebe, Influence of manganese ions on cellular behavior of human osteoblasts in vitro, Biomol. Eng. 24 (2007) 531–536.

[36] J. Xiao, S. Chen, J. Yi, H. Zhang, G.A. Ameer, A cooperative copper metal-organic framework-hydrogel system improves wound healing in diabetes, Adv. Funct. Mater. 27 (2017) 1604872.

[37] H. Yue, L. Zhou, R. Zou, Z. Li, T. Liao, J. Yan, Y. Zhou, M. Yang, Z. Piao, Promotion of skin fibroblasts collagen synthesis by polydioxanone mats combined with concentrated growth factor extracts, J. Biomater. Appl. 34 (2019) 487–497.

[38] Y. Ni, Y. Ju, H. Ohi, Further understanding of the manganese-induced decomposition of hydrogen peroxide, J. Pulp Pap. Sci. 26 (2000) 90–94.

[39] J. Zhou, M. Li, Y. Hou, Z. Luo, Q. Chen, H. Cao, R. Huo, C. Xue, L. Sutrisno, L. Hao, Y. Cao, H. Ran, L. Lu, K. Li, K. Cai, Engineering of a nanosized biocatalyst for combined tumor starvation and low-temperature photothermal therapy, ACS Nano 12 (2018) 2858–2872.

[40] O. Warburg, On the origin of cancer cells, Science 123 (1956) 309–314.

[41] K.J. Henle, L.A. Dethlefsen, Heat fractionation and thermotolerance: a review, Canc. Res. 38 (1978) 1843–1851.

[42] G. Hegyi, G.P. Szigeti, A. Szasz, Hyperthermia versus oncothermia: cellular effects in complementary cancer therapy, evid. Based complement, Alternative Med. 2013 (2013) 672873.

[43] H. Ma, C. Jiang, D. Zhai, Y. Luo, Y. Chen, F. Lv, Z. Yi, Y. Deng, J. Wang, J. Chang, C. Wu, A bifunctional biomaterial with photothermal effect for tumor therapy and bone regeneration, Adv. Funct. Mater. 26 (2016) 1197–1208.

[44] Q. Yu, Y. Han, T. Tian, Q. Zhou, Z. Yi, J. Chang, C. Wu, Chinese sesame stick-inspired nano-fibrous scaffolds for tumor therapy and skin tissue reconstruction, Biomaterials 194 (2019) 25–35.

[45] D.K. Kirui, D.A. Rey, C.A. Batt, Gold hybrid nanoparticles for targeted phototherapy and cancer imaging, Nanotechnology 21 (2010) 105105.

[46] C. Lee, C. Hong, H. Kim, J. Kang, H.M. Zheng, TiO₂ nanotubes as a therapeutic agent for cancer thermotherapy, Photochem. Photobiol. 86 (2010) 981–989.

[47] Z.M. Markovic, L.M. Harhaji-Trajkovic, B.M. Todorovic-Markovic, D.P. Kepic, K. M. Arsikin, S.P. Jovanovic, A.C. Pantovic, M.D. Dramicanin, V.S. Trajkovic, In vitro comparison of the photothermal anticancer activity of graphene nanoparticles and carbon nanotubes, Biomaterials 32 (2011) 1121–1129.

[48] B. Liu, Z. Wang, T. Li, Q. Sun, P. Yang, Rapid decomposition and catalytic cascade nanoplatforms based on enzymes and Mn-etched dendritic mesoporous silicon for MRI-guided synergistic therapy, ACS Appl. Mater. Interfaces 12 (2020) 45772–45788.

[49] X. Wang, F. Lv, T. Li, Y. Han, Z. Yi, M. Liu, J. Chang, C. Wu, Electrospun micropatterned nanocomposites incorporated with Cu2S nanoflowers for skin tumor therapy and wound healing, ACS Nano 11 (2017) 11337–11349.